ACS OMEGA

Open Access

http://pubs.acs.org/journal/acsodf

Article

Evolution of Karst Geothermal Hydrochemical Characteristics and Genesis Mechanism in Northern Jinan, Shandong, Eastern China

Shuchun Wang, Zhiqing Liu, Wei Zhou,* Yanyu Jiang, Hongliang Ding, and Fangying Dong

Cite This: *ACS Omega* 2024, 9, 36299−36313

Read Online

ACCESS | Metrics & More | Article Recommendations

ABSTRACT: The study of geothermal water hydrochemical characteristics and solute transport evolution can provide a reliable hydrogeochemical basis for the development and protection of geothermal resources. Currently, there is a lack of systematic research on the hydrochemical evolution mechanism of geothermal fields in northern Jinan, which limits the development and use of geothermal fields. In this study, the hydrochemical properties of groundwater in northern Jinan were described by analyzing the hydrochemical characteristics of 16 geothermal water samples and 3 cold water samples. The results show that during the transformation from cold water in the south to geothermal water in the north, the contents of major ions all show an increasing trend and the hydrochemical characteristics show obvious zoning characteristics. The hydrochemical type evolved from HCO_3−Ca to HCO_3−Ca·Mg type, and then further evolved SO_4−Ca and SO_4−Ca·Na type water. Dissolution−precipitation of carbonate, sulfate, halite, and silicate minerals is one of the important processes that controls the chemical characteristics of geothermal water. The water source is mainly from the atmospheric precipitation in the Taiyi Mountain, with an altitude of 698.99−1464.91 m.s.a.l. The thermal reservoir temperature in the study area is estimated to be 55.62−98.16 °C. This paper proposes a conceptual model of the karst geothermal water flow system in northern Jinan, which provides a new idea for exploring the geothermal water genesis mechanism under similar geological conditions.

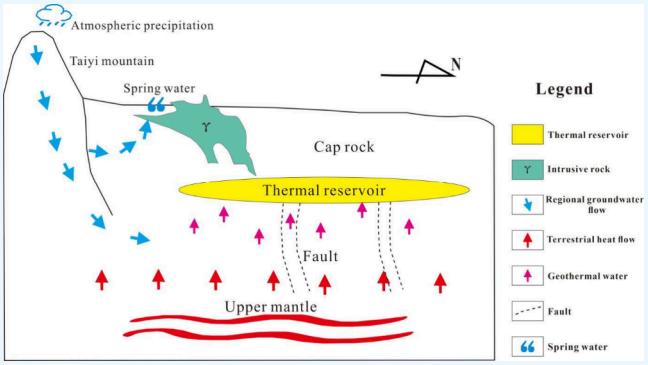

1. INTRODUCTION

With energy and environmental problems becoming more and more prominent, geothermal energy as a renewable energy has received more and more attention. Extensive geothermal development is underway worldwide,[1,2] including the United States, Turkey, Germany, Spain, and China. Compared with traditional fossil energy, geothermal resources have the advantages of cleanliness,[3−7] high efficiency, stability, safety, and latent enormous economic value.[2] Understanding the hydrochemical evolution mechanism of geothermal water is a prerequisite and foundation for the rational development of geothermal resources. Therefore, it is necessary to study the hydrochemical characteristics and evolution mechanism of geothermal water.

Currently, there are scaling and corrosion problems in the utilization of geothermal water due to the effect of solutes in the groundwater, resulting in a decrease in the utilization rate of geothermal energy.[8,9] Therefore, we need more research and analysis of solutes in groundwater. Groundwater geochemical processes have been widely used in studies of solute evolution in groundwater systems.[10−14] The use of major chemical ions as tracers to analyze hydrochemical processes of aquifers is a rapid and scientifically effective method, including multivariate statistical methods and hydrogeochemical simulation.[15] Multivariate statistics are often used to quantitatively analyze complex relationships between things.[16,17] This specifically involves Principal Component Analysis (PCA), Factor Analysis (FA), Hierarchical Cluster Analysis (HCA), and Correlation Analysis (CA). Among them, PCA, which is mainly based on the idea of "dimensionality reduction", replacing multiple indicators with a few comprehensive indicators, is increasingly being used to assess the quality of groundwater and analyze factors affecting groundwater.[18,19] Interpretation of the hydrochemical mechanisms controlling the origin of water constituents combines statistical methods with hydrochemical analysis.[20] Hydrogeochemical simulation is mainly studied with the help of hydrogeochemical models, including the component distribution model (WATEQ, EQ), mass balance model (MT3DMS), and reaction path model (PHREEQC). PHREEQC is capable of better tracking the direction of

Received: March 25, 2024
Revised: August 7, 2024
Accepted: August 8, 2024
Published: August 16, 2024

https://doi.org/10.1021/acsomega.4c02870
ACS Omega 2024, 9, 36299−36313

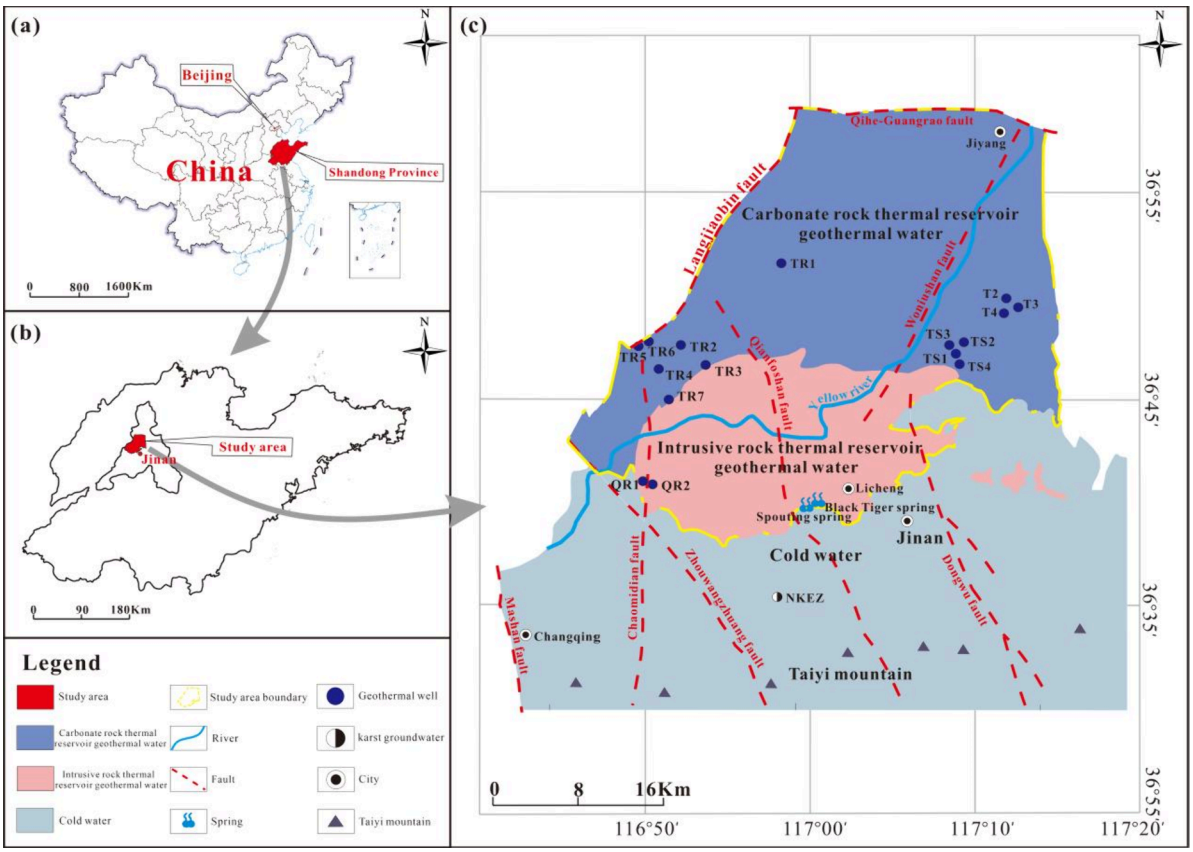

Figure 1. Study area and sampling point: (a) Map of China. (b) Location map of northern Jinan. (c) Study area and sampling point location.

groundwater flow and the saturation state of minerals, and can carry out the calculation of mineral saturation index (SI) and the study of reverse geochemical simulation, which have attracted the attention of a wide range of scholars for its advantages in analyzing chemical reactions and solute transport.[21,22] Mutual verification of PCA and PHREEQC simulation results allows for a more accurate analysis of mineral dissolution−precipitation effects, which can lead to a better study of the water−rock interaction that occurs during groundwater runoff and improves the utilization of geothermal resources.

Karst geothermal water is widely distributed around the world and is a very important geothermal resource.[7,23] At present, numerous scholars have carried out a great deal of research. The source of karst water recharge is determined by isotopes and chemical ions, and the degree of karst water−rock interaction and mixing is identified.[24,25] The flow path of karst geothermal water is analyzed by temperature and conductivity to analyze the karst development pattern and major hydrogeological problems.[26] To understand the flow pattern of karst geothermal water, the key is to study the evolution process of geothermal fluid and construct a conceptual model of the karst geothermal water genesis pattern. The object of this study is karst geothermal water in the north of Jinan. Since the 21st century, geophysical exploration and geothermal measurements of temperature boreholes have been carried out in this area, but relatively little research has been carried out on the hydrochemical characteristics of geothermal water and on the mechanism of its genesis. This situation has led to the underdevelopment of karst geothermal resources in northern Jinan, and a complete development and utilization system has not yet been formed.

In this context, this study samples and compares carbonate rock thermal reservoir geothermal water, intrusive rock thermal reservoir geothermal water, and cold water in Jinan. The objectives are as follows: (1) Revealing the hydrochemical characteristics and other properties of the groundwater; (2) Elucidating the geochemical sources of the major ions in the groundwater and their associated hydrogeochemical processes; (3) Exploring the mechanism of the formation of karst geothermal water in the northern part of Jinan, and proposing a karst geothermal flow system conceptual model.

2. STUDY AREA

2.1. Hydrogeological Characteristics. The study area involves three counties and districts, Changqing District, Jiyang County, and Licheng District, Jinan City, bounded by the Qihe-Guangrao rupture in the north and the Jinan rocky body in the south, with geographic coordinates ranging from 116°46′ E to 117°20′ E, and 36°40′ N to 36°59′ N, and covering an area of 1,399 km^2 (Figure 1). The climate in the region is classified as a warm-temperate continental climate, with an average annual temperature of 14.7 °C. The average annual precipitation is 705.56 mm, of which 70% occurs in the July−September period. The main rivers in the area are the Yellow River, the Xiaoqing River, and the trunk canal of the Yellow River. This area belongs to the combination of the Piedmont alluvial plain and the Yellow River alluvial plain, developing two sets of faults (NNE and NNW), and the terrain is high in the south and low in the north. The water-bearing rock group in the study area is mainly composed of loose rock

https://doi.org/10.1021/acsomega.4c02870
ACS Omega 2024, 9, 36299−36313

Table 1. Main Hydrochemical Parameters and Descriptive Statistics in the Study Area[a]

Sample category	Sample number	Well depth (m)	pH	Temperature (°C)	TDS	K^+	Na^+	Ca^{2+}	Mg^{2+}	Cl^-	SO_4^{2-}	HCO_3^-	F^-	SiO_2	%CBE
Carbonate rock thermal reservoir geothermal water	T2	792.78	7.30	39.0	7273.14	70.00	1400.00	863.05	149.99	2369.24	2276.20	110.65	3.00	26.00	1.00%
	T3	770.41	7.31	40.0	7079.02	62.50	1400.00	810.43	143.61	2303.29	2217.23	110.65	2.70	23.00	0.91%
	T4	814.00	7.18	43.0	7268.71	71.25	1425.00	847.26	146.80	2369.24	2264.40	110.65	3.00	26.00	1.13%
	TS1	572.43	7.10	33.0	5233.04	34.00	725.00	762.01	157.02	1303.84	2063.91	162.90	3.25	19.00	0.71%
	TS2	782.77	7.70	36.0	5142.34	31.75	737.70	736.75	159.57	1273.40	2004.94	175.19	2.80	18.00	1.54%
	TS3	806.30	7.23	38.0	5035.19	34.72	714.29	705.24	140.42	1330.31	1923.04	161.77	2.40	22.75	−0.80%
	TS4	576.90	7.60	35.7	1950.59	16.61	250.00	284.57	65.39	452.82	634.51	224.39	2.30	19.75	2.18%
	TR1	1800.56	7.38	56.0	3537.56	28.00	350.00	556.77	121.89	274.90	2006.20	166.30	3.50	24.95	1.57%
	TR2	1312.34	7.11	43.0	3355.31	18.10	132.25	637.70	148.30	114.62	2101.85	180.21	2.75	22.90	0.48%
	TR3	419.10	7.70	33.0	2437.98	11.88	100.00	480.57	110.03	113.96	1414.00	191.50	1.97	22.21	2.77%
	TR4	904.95	7.65	43.2	3167.36	18.23	200.00	569.14	108.26	241.76	1815.66	185.25	3.75	27.00	−1.09%
	TR5	1601.57	7.17	57.0	3424.56	23.00	245.00	598.60	128.71	342.10	1905.94	154.10	3.50	27.00	0.03%
	TR6	1734.19	7.07	55.5	3284.15	19.08	140.50	640.86	138.07	136.36	2006.87	174.10	–	–	1.66%
	TR7	643.64	7.70	38.0	1418.53	9.40	88.00	234.71	62.55	97.41	684.04	218.22	1.60	21.00	1.07%
Intrusive rock thermal reservoir geothermal water	QR1	770.68	8.20	25.2	516.99	3.13	73.33	35.35	18.22	35.82	158.63	146.12	0.20	46.20	−1.17%
	QR2	1002.60	7.81	27.5	452.00	2.75	16.67	60.98	21.97	17.91	43.93	268.75	0.20	18.56	−1.31%
Southern cold water	NKEZ	–	7.94	14.0	366.22	0.61	4.50	97.77	15.61	12.70	81.56	259.34	0.18	9.49	0.73%
	Spouting Spring	–	7.23	16.0	421.89	1.17	18.11	103.40	18.09	38.83	71.74	262.39	0.21	13.76	4.21%
	Black Tiger Spring	–	7.70	15.0	521.60	1.05	25.73	118.90	21.09	55.61	94.91	299.00	0.20	14.48	2.33%

[a]Note: – are no available data, except pH, units for concentrations are mg/L.

https://doi.org/10.1021/acsomega.4c02870
ACS Omega 2024, 9, 36299−36313

pore water, mainly composed of Quaternary and Neogene loose deposits.[24]

2.2. Geothermal Geological Setting. The study area is part of the northern wing of the Taishan uplift. The Paleozoic period is widely distributed, and the geothermal fluid mainly occurs in the Ordovician limestone thermal reservoir. The thermal reservoir type is mainly carbonate fractured karst thermal reservoir, including the Ordovician Majiagou Group and Cambrian system, with lithology dominated by limestone and dolomite. The Ordovician limestone thermal reservoir is characterized by a layered and banded thermal reservoir, controlled by fracture structures with complex geological and tectonic conditions. According to the geothermal well (TS4) data, it is known that the top boundary of the Ordovician limestone thermal reservoir is buried at a depth of 190−2500 m with a thickness of about 800 m. The cap rock of the thermal reservoir is Quaternary, Neogene, Permian, and Carboniferous, which plays a thermal insulation role in the Ordovician Majiagou Group limestone thermal reservoir with a thickness of 210−2450 m.

The magmatic activity in the southern region is more intense, mainly in the late Mesozoic IndoChin-Yanshan movement, forming the "Jinan rock mass" dominated by gabbro and supplemented by diorite, which belongs to the type of intrusive rock thermal reservoir. According to the geothermal well (QR1, QR2) data, it is known that the thermal reservoir cap rock is Quaternary, and the thickness is generally 200−250 m.

As shown in Figure 1, karst groundwater flows from the south to the north, which coincides with the topography. To a certain extent, the "Jinan rock mass" blocks a large amount of cold water runoff to the north, causing part of the karst water to circulate deep underground, thus increasing the temperature of the geothermal fluid in the north. The developed faults in the study area serve as conduits for the rising heat flow and deep circulation convection. Therefore, this unique geological environment creates favorable conditions for the formation of geothermal heat.

3. MATERIALS AND METHODS

3.1. Sample Collection and Testing. Around 2022, a total of 19 water samples were collected in the study area. Among them are 14 carbonate reservoir geothermal water samples, 2 intrusive rock reservoir geothermal water samples, and 3 cold water samples (Ordovician karst water and spring water in the south of the geothermal field). The position of each sampling point is shown in Figure 1. Each sample is tested for major cations (Ca^{2+}, Mg^{2+}, K^+, Na^+), major anions (HCO_3^-, Cl^-, SO_4^{2-}, F^-), SiO_2, and pH in the Shandong Geological and Mineral Engineering Survey Institute. The results for each sample are given in Table 1. This testing center has a strict quality control system that incorporates national standards. In order to ensure the accuracy of data, the charge balance error (% CBE) is calculated for all samples.[27−29] The % CBE values for all samples are within ±5%, indicating that the groundwater quality data in the study area are reliable. The % CBE values of all samples are within ±5%, indicating that the test results of water samples in the study area are reliable.

$$\%\mathrm{CBE} = \frac{\sum \text{cation} - \sum \text{anion}}{\sum \text{cation} + \sum \text{anion}} \times 100 \quad (1)$$

3.2. Principal Component Analysis. PCA is the rearrangement of a set of correlated variables into new uncorrelated components with little loss of information.[30,31] Each principal component is a linear combination of the original variables, and the principal components are not related to each other. The basic idea of PCA is that these principal components can explain the relationship between the original variables and can be used to study groundwater chemical sources and groundwater quality.[32] The general steps of principal component analysis include: (1) collecting water sample data, (2) data standardization, (3) establish the correlation coefficient matrix, (4) calculate the covariance matrix, (5) calculation of principal components, and (6) select and interpret principal components. The number of principal components is based on the Kaiser criterion, and the cumulative variance contribution of the correlation matrix is greater than 80%, and the eigenvalue is greater than 1.0.[33] IBM SPSS data software was used for statistical analysis to check whether there was a correlation between the data in advance. Among them, the KMO value should be >0.6, and the Sig value of the Bartlett sphericity test should be <0.05.[34] Standardizing the data set using a Z-score method before PCA analysis reduces errors.[30] The Z-score is calculated using eq 2:

$$Z = \frac{X - \overline{X}}{S} \quad (2)$$

where X represents the observed value of the chemical parameter, $\overline{X}$ represents the mean value of the chemical index, and S represents the standard deviation.

3.3. Chemical Simulation Technology. Hydrogeochemical simulation studies the geochemical processes of water−rock interactions, mainly including forward and reverse geochemical simulation.[35] Based on available hydrochemical data, reverse geochemical simulation is used to determine the water−rock reactions occurring in the groundwater system and to solve the problem of geochemical evolution path in the groundwater flow field.[36,37] PHREEQC is a typical representative of hydrogeochemical simulation software with reverse geochemical simulation functions.[21−23] The hydrochemical indexes of the start and end points of the reaction path are input into the corresponding module of PHREEQC, and the model is run after the corresponding minerals. Due to the relatively large number of minerals involved, the model simulation results have multiple solutions. Therefore, it is necessary to comprehensively analyze the mineral composition characteristics of rock samples and the basic law of the hydrolysis reaction of silicate minerals, adjust the parameters and uncertainty, and then select the actual path. The leading theory used in hydrogeochemical simulation in this paper is the equilibrium equation for the mineral dissolution−precipitation reaction.

$$\sum_{j=1}^{I} b_{p\cdot j} \cdot \lg a_j = \lg K_p \quad (3)$$

where a_j represents the activity of the free ions in the noncomplex in the jth, $b_{p\cdot j}$ represents the stoichiometric number of free ions in the jth mineral in the pth mineral, I represents the middle number in the water-soluble substances, J represents the number of free ions, and K_p represents the equilibrium constant of the (dissolution) reaction of the pth mineral phase.

https://doi.org/10.1021/acsomega.4c02870
ACS Omega 2024, 9, 36299−36313

4. RESULTS AND DISCUSSION

4.1. Groundwater Hydrochemical Characteristics. Groundwater in northern Jinan exhibits a medium-low temperature range of 25.2−57.0 °C. The main ionic components in groundwater are Na^+, K^+, Ca^{2+}, Mg^{2+}, Cl^-, SO_4^{2-}, HCO_3^- and TDS, with concentrations ranging from 16.62 to 1425.00 mg/L, 2.75−71.25 mg/L, 35.35−863.05 mg/L, 21.97−159.57 mg/L, 17.91−2369.24 mg/L, 43.93−2276.20 mg/L, 110.65−268.75 mg/L, 452.00−7273.14 mg/L, respectively. The pH value is 7.07−8.20, which is weakly alkaline.

In this paper, a box diagram of ion concentration was adopted to analyze the ion concentration distribution, as shown in Figure 2. The average concentration of cations in

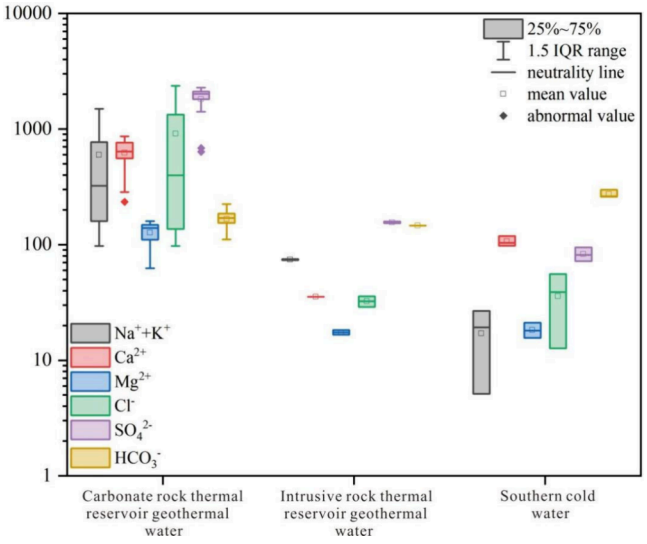

Figure 2. Chemical component box diagram of the water sample.

carbonate rock thermal reservoir geothermal water is Ca^{2+} > K^++Na^+ > Mg^{2+}, and the average concentration of anions is SO_4^{2-} > Cl^- > HCO_3^-. The average concentration of cations in intrusive rock thermal reservoir geothermal water is K^++Na^+ ≥ Ca^{2+} > Mg^{2+}, and the average concentration of anions is HCO_3^- > SO_4^{2-} > Cl^-. The average concentration of cations in southern cold water is Ca^{2+} > K^++Na^+ > Mg^{2+}, and the average concentration of anions is HCO_3^- > SO_4^{2-} > Cl^-. Obviously, the average concentrations of cations and anions in different regions are different, indicating that critical hydrogeochemical processes occur during groundwater flow.

The Piper diagram is commonly used in hydrochemical analysis and classification to illustrate hydrogeochemical phenomena.[38−40] Figure 3 shows the Piper diagram of groundwater in the study area. The groundwater hydrochemical type shows obvious zoning characteristics from southern cold water to northern geothermal water. The hydrochemical characteristics of southern cold water are stable, the overall variability is not apparent, and the hydrochemical type is mainly HCO_3−Ca. The hydrochemical type of intrusive rock thermal reservoir geothermal water is mainly HCO_3−Ca·Mg. The hydrochemical types of carbonate rock thermal reservoir geothermal water vary widely, mainly SO_4−Ca and SO_4−Ca·Na, and the hydrochemical types of some water samples (T2, T3, and T4) are SO_4·Cl−Ca·Na and Cl·SO_4−Na·Ca. Among the groundwater samples collected, the carbonate rock thermal reservoir geothermal water has the highest TDS content and the most significant difference in water quality, leading to speculation of a relatively closed hydrogeochemical environment with slow runoff.

4.2. Geothermal Fluid Evolution. *4.2.1. Water−Rock Interactions Revealed by PCA.* PCA is used for statistical analysis of geothermal and cold water together to determine the main geochemical processes of chemical composition formation.[15,20] According to the PCA results, the KMO and Bartlett ball values were 0.731 and 451.467, respectively, and the sig value was 0.0, which met the requirements. Therefore, the data were suitable for PCA analysis. In this study, PCA identified three principal components (PC) that explained 95.21% of the total cumulative variance (Table 2). PC1 accounts for the majority of the total variance (73.63%) and represents the salinity component. Among them, TDS (0.98), K^+ (0.94), Na^+ (0.89), Ca^{2+} (0.98), Mg^{2+} (0.93), Cl^- (0.87), SO_4^{2-} (0.95), HCO_3^- (−0.88), and F^- (0.83) have a strong load. SiO_2 (0.25) has the lowest load. F^- is generally strongly correlated with Na^+, and its concentration is easily affected by Ca^{2+} and HCO_3^-.[41] PC2 accounts for 12.00% of the total variance and has a high load (0.92) on the SiO_2 value, which represents the effect of silicate on groundwater. PC3, which accounts for 9.58% of the total variance, has a positive load at pH (0.48), representing the effect of pH on solute dissolution in groundwater.

4.2.1.1. Salinity Component (PC1). According to Figure 4a, the average value of $r(Cl^-)/r(K^+{+}Na^+)$ of the geothermal and cold water samples in the study area is 0.90, which is distributed along the 1:1 distribution and close to the line of halite dissolution, indicating that $Na^+(K^+)$ and Cl^- mainly originate from the dissolution of halite. The $Na^+(K^+)$ and Cl^- solubilities of the cold water are much lower than those of the geothermal water, indicating that the weathering and dissolution of halite in geothermal water is stronger.

As shown in eq 7, gypsum dissolution releases $r(Ca^{2+})$:$r(SO_4^{2-})$ = 1:1 in geothermal water. According to Figure 4b, the value of $r(Ca^{2+})/r(SO_4^{2-})$ in the geothermal water samples is 0.91, which is close to 1, indicating that gypsum dissolution is the main source of Ca^{2+} and SO_4^{2-} in geothermal water. Except for the TS4 water sample, the geothermal water samples are all located above the gypsum dissolution line, indicating that SO_4^{2-} in geothermal water may be derived from H_2S in deep hot water or oxidation of sulfur-containing minerals in addition to gypsum dissolution.[42,43]

From eqs 8 and 9, calcite dissolves $r(Ca^{2+})$:$r(HCO_3^-)$ = 1:1, and dolomite dissolves $r(Ca^{2+})$:$r(Mg^{2+})$:$r(HCO_3^-)$ = 1:1:2. $r(Ca^{2+}{+}Mg^{2+})/r(HCO_3^-)$ = 1:1. In Figure 4c, this indicates the trend of dissolution−precipitation of calcite or dolomite. The values of $r(Ca^{2+}{+}Mg^{2+})/r(HCO_3^-)$ in the geothermal waters of the study area ranged from 1.32 to 30.68, with a mean value of 15.01, which is much larger than 1, indicating that gypsum dissolution is more dominant compared with calcite and dolomite. Meanwhile, PC1 has high loading on HCO_3^- (−0.88), suggesting that the continuous dissolution of gypsum may inhibit the dissolution of calcite or dolomite.

Figure 4d shows that geothermal water is further away from the origin than cold water, indicating that the ion exchange of geothermal water is greater than that of cold water, and the water−rock interaction of geothermal water is more intense.[44] Almost all water samples are distributed along a $y = -x$ straight line with a decreasing trend, and R^2 = 0.90 indicates that the cation exchange process is relatively strong. On the other hand, according to previous studies, the distribution of modern

https://doi.org/10.1021/acsomega.4c02870
ACS Omega 2024, 9, 36299−36313

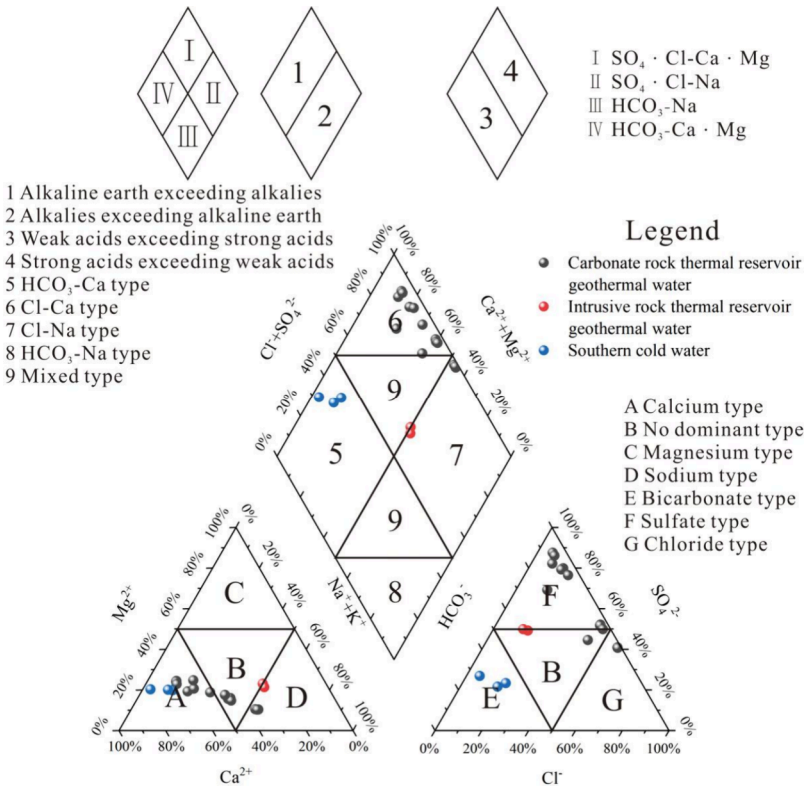

Figure 3. Piper diagram of the water samples.

Table 2. Principal Components of Geothermal Water and Cold Water Samples

Indices	Components		
	1	2	3
TDS	0.98	−0.05	0.16
K^+	0.94	0.24	0.31
Na^+	0.89	0.18	0.45
Ca^{2+}	0.98	−0.11	−0.11
Mg^{2+}	0.93	−0.10	−0.27
Cl^-	0.87	−0.02	0.49
SO_4^{2-}	0.95	−0.40	−0.28
HCO_3^-	−0.88	−0.45	0.03
F^-	0.83	−0.05	−0.47
SiO_2	0.25	0.92	−0.20
pH	−0.47	0.26	0.48
Eigenvalue	8.10	1.32	1.05
Variance (%)	73.63	12.00	9.58
Cumulative (%)	73.63	85.63	95.21

infiltrating water is generally near the origin.[45] It can be found in Figure 4e that both cold water and intrusive rock thermal reservoir geothermal water have a close hydraulic relationship with modern permeable water. In summary, compared to cold water, geothermal water has a longer residence time in thermal reservoirs, participates more deeply in the water cycle, and has a more significant cation exchange effect.[46]

4.2.1.2. Silicate Composition (PC2). The weathering dissolution of evaporite, silicate, and carbonate minerals is a common form of water−rock interaction, which can be distinguished by Mg/Na and Ca/Na.[47] Figure 5 shows that the geothermal water samples are concentrated in the area of silicate weathering and dissolution, and some of them are in the transition area between silicate and carbonate, indicating that geothermal water is mainly subjected to the weathering and dissolution of silicate minerals. Therefore, the SiO_2 content in the geothermal water mainly originates from the dissolution of silicate minerals. The solubility is proportional to the temperature, and it is not easy to precipitate with the decrease of the temperature, so it can be used to calculate the thermal reservoir temperature under certain circumstances.[48]

4.2.1.3. Effect of pH on Mineral Dissolution (PC3). PC1 and PC3 are utilized to generate a PCA biplot for groundwater (Figure 6). This biplot can be used to analyze the correlation between the main components.[49] In a PCA biplot, the cosine value of the angle between any two arrows represents the correlation between two variables, and two orthogonal arrows represent components that are independent of each other.

The results show that the pH parameter is approximately orthogonal to Cl^- and Na^+, indicating that the pH may be independent of Cl^- and Na^+, suggesting that the dissolution of halite does not affect the magnitude of the pH. Halite dissolution is one of the sources of higher salinity in geothermal water. As shown in Figure 6, the angle between pH and SO_4^{2-} is greater than 90°, and the cosine value is negative, indicating that pH is negatively correlated with sulfate dissolution. The desulfurization coefficient ($100 \times rSO_4^{2-}/rCl^-$) is 70.69−1356.21, far greater than the desulfurization coefficient of normal seawater (10.2), indicating that the geothermal water is in a reducing environment, and desulfurization is easy to be carried out, thus reducing the concentration of SO_4^{2-} and increasing the pH of the water.

4.2.2. Water−Rock Interactions Revealed through Gibbs Diagrams. The Gibbs diagram is used to study the controlling factors for the formation of major ions in groundwater by utilizing the relationship between Na^+, Ca^{2+}, Cl^-, HCO_3^- and

https://doi.org/10.1021/acsomega.4c02870
ACS Omega 2024, 9, 36299−36313

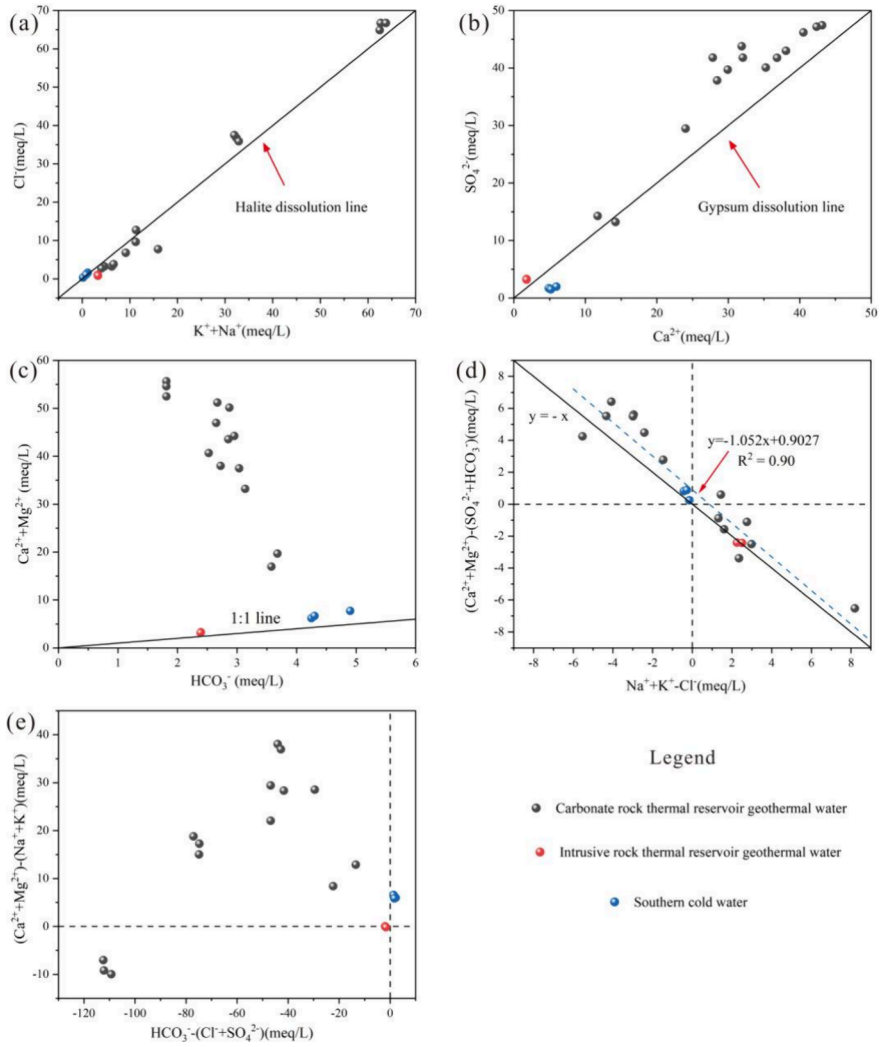

Figure 4. Scatter plots of (a) Cl^- versus Na^++K^+. (b) SO_4^{2-} versus Ca^{2+}. (c) HCO_3^- versus Ca^{2+}+Mg^{2+}. (d) (Ca^{2+}+Mg^{2+})-(SO_4^{2-}+HCO_3^-) versus (Na^++K^+-Cl^-). (e) (Ca^{2+}+Mg^{2+})-(Na^++K^+) versus HCO_3^--(Cl^- + SO_4^{2-}) in geothermal water samples and cold water samples.

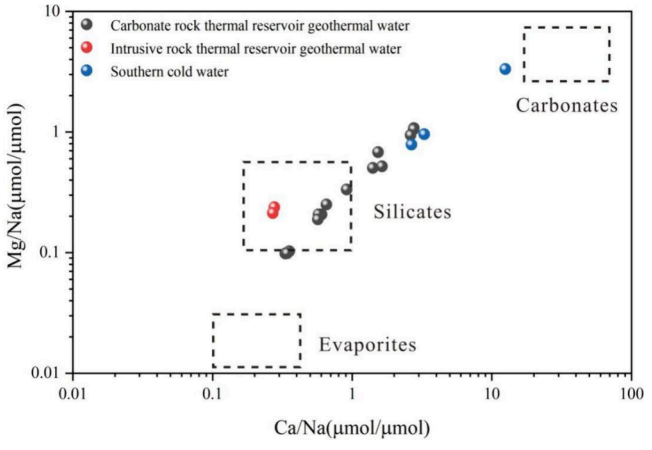

Figure 5. Scatter diagram of Mg/Na versus Ca/Na in the geothermal water samples and cold water samples. The dashed box represents the global average of different weathering mechanisms (silicate, carbonate, and evaporate dissolution).

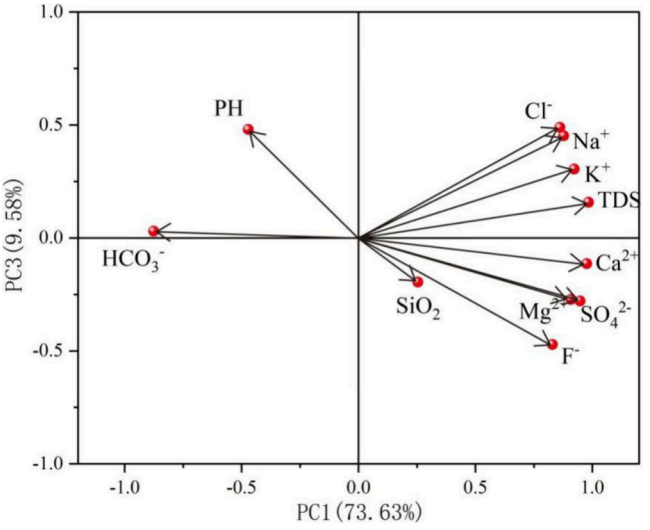

Figure 6. Biplot of the component loadings for the first two components.

TDS in water, including three types: evaporation concentration-controlled, rock weathering-controlled, and precipitation action-controlled.[50] In recent years, researchers have widely utilized Gibbs diagrams to study the formation role of geothermal water.[27,51]

https://doi.org/10.1021/acsomega.4c02870
ACS Omega 2024, 9, 36299−36313

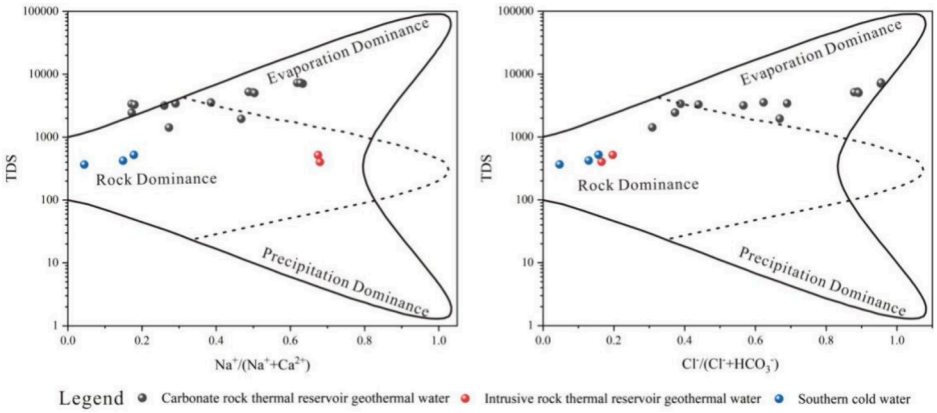

Figure 7. Gibbs diagram of the water sample in the study area.

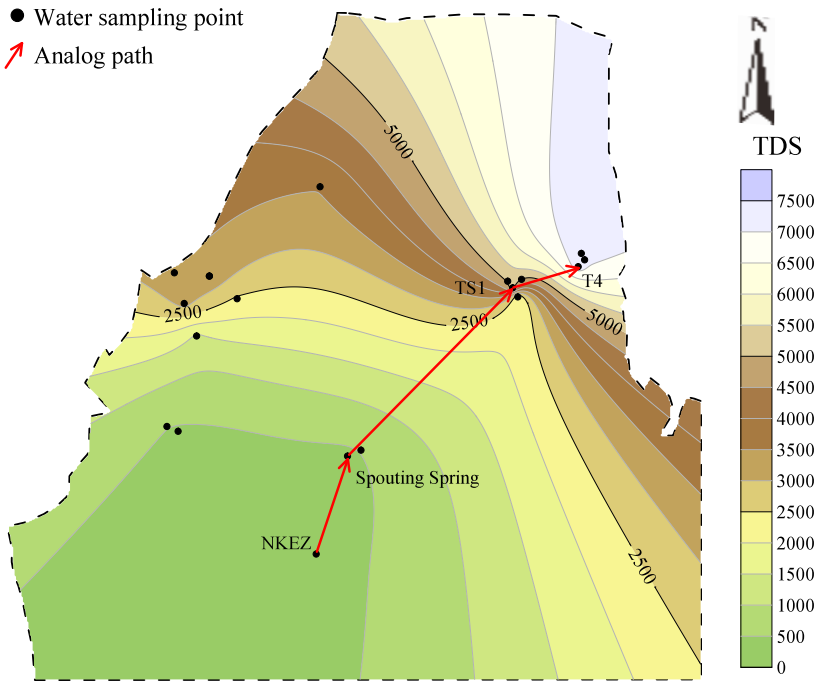

Figure 8. TDS spatial distribution and path map in the study area.

The formation role of groundwater in the study area is analyzed using the Gibbs diagram (Figure 7). The TDS of groundwater samples is 452.00−7273.14 mg/L, the $Na^+/(Na^+ + Ca^{2+})$ value is in the range of 0.04−0.67, and the $Cl^-/(Cl^- + HCO_3^-)$ value is in the range of 0.04−0.96. As shown in Figure 7, the ratios of $Na^+/(Na^+ + Ca^{2+})$ and $Cl^-/(Cl^- + HCO_3^-)$ gradually increase from southern cold water to northern geothermal water. It is speculated that the reason is that the concentrations of Ca^{2+} and HCO_3^- in geothermal water gradually decrease, and the evaporation and concentration gradually replace the weathering and dissolution of rocks and become the primary control factor. Enhanced evaporation causes a large amount of water to be lost, and the salts in the aqueous solution are retained in the thermal reservoir, which accumulates for a long period of time causing the TDS of the geothermal water to rise.

4.2.3. Water−Rock Interactions Revealed by Reverse Geochemical Modeling. 4.2.3.1. Reaction Path Determination. The study area is located in the geothermal area of the central Shandong Province, where the geothermal fields have complex geological characteristics due to more intense magmatic activities. Along the direction of groundwater runoff, there is an overall increasing trend in TDS values as hydrogeochemistry continues. According to the law of change of TDS of water samples in the study area, combined with the direction of groundwater flow, a groundwater runoff path is selected for simulation, and the spatial variation rule of TDS and the path diagram in the study area are drawn (Figure 8). As a whole, the groundwater sample flowing through this path is NKEZ → Spouting Spring → TS1 → T4.

4.2.3.2. Possible Mineral Phase Chemical Reactions. Through the analysis of geothermal geological conditions, it is known that the lithology of the Ordovician strata in the study area is mainly chert and dolomite. The main mineral components of the rock are calcite, dolomite, quartz, feldspar, and small amounts of glauconite and clay minerals. The water−rock reaction in geothermal water mainly includes the dissolution of minerals, such as halite, gypsum, calcite, dolomite, quartz, and feldspar. During the reaction, secondary minerals, such as gibbsite and kaolinite, are generated.

https://doi.org/10.1021/acsomega.4c02870
ACS Omega 2024, 9, 36299−36313

Therefore, halite, albite, k-feldspar, quartz, gypsum, calcite, dolomite, and kaolinite are selected as the mineral phases for possible reactions. The reaction chemical equations are as follows:

The dissolution of feldspar:

$$2NaAlSi_3O_8 + 9H_2O + 2H_2CO_3 \rightarrow 2Na^+ + Al_2Si_2O_5(OH)_4 + 4H_4SiO_4 + 2HCO_3^- \quad (4)$$

$$2KAlSi_3O_8 + 9H_2O + 2H_2CO_3 \rightarrow 2K^+ + Al_2Si_2O_5(OH)_4 + 4H_4SiO_4 + 2HCO_3^- \quad (5)$$

The dissolution of quartz:

$$SiO_2 + 2H_2O \rightarrow H_4SiO_4 \quad (6)$$

The dissolution of gypsum:

$$CaSO_4 \cdot 2H_2O \rightarrow Ca^{2+} + SO_4^{2-} + 2H_2O \quad (7)$$

The dissolution of calcite and dolomite:

$$CaCO_3 + H_2O \rightarrow Ca^+ + HCO_3^- + OH^- \quad (8)$$

$$CaMg(CO_3)_2 + 2H_2O \rightarrow Ca^+ + Mg^{2+} + 2HCO_3^- + 2OH^- \quad (9)$$

4.2.3.3. Hydrogeochemical Simulation Results. Since the dissolution of carbonate minerals requires the participation of CO_2, $CO_2(g)$ is added to the model. The incomplete dissolution of silicate minerals produces kaolinite, so kaolinite is added to the model.[52] The results of this reverse geochemical simulation are shown in Table 3.

Combined with the above research results, due to the long reaction path, the hot water in the deep thermal reservoir may have experienced complex chemical reaction processes such as halite weathering, evaporation, and concentration before reaching the surface, and the TDS, ionic characteristics, and hydrochemical type evolution characteristics of the geothermal field have changed significantly. Therefore, the simulation calculation shows that a series of complex water−rock reactions has been experienced on the reaction path. In southern cold water, the groundwater is close to the recharge area, the burial is shallow, the karst fissures are more developed, and the groundwater runoff is faster. Thus, since the NKEZ-Spouting Spring, the hydrochemical composition has not changed much, and all kinds of minerals dissolved are not more than 1×10^{-03}.

Due to the obstruction of the overlying rock mass, the path from Spouting Spring to TS1 is characterized by an increase in the depth of groundwater burial, a stagnation of runoff, a significant increase in the water−rock interaction, and a significant increase in the number of dissolved minerals of various types. In this path, gypsum has been in an unsaturated state, leading to a large dissolution of gypsum and an increase in the Ca^{2+} ion concentration. The solubility of gypsum is much greater than that of calcite, which inhibits the dissolution of calcite and further leads to the precipitation of calcite, and the dolomite remains in a dissolved state. The dissolution of albite and k-feldspar increases, producing secondary minerals such as kaolinite. At the same time, due to the large difference in the quality of carbonate rock thermal reservoir geothermal water, with the highest TDS, and the increase in the depth of

Table 3. Results of the Inverse Geochemical Model[a]

Path	Albite	K-feldspar	Calcite	Dolomite	Gypsum	Halite	Quartz	Kaolinite	CO_2
NKEZ-Spouting Spring	5.33×10^{-06}	1.43×10^{-05}	5.78×10^{-05}	7.21×10^{-05}	4.28×10^{-05}	6.42×10^{-04}	-1.07×10^{-05}	-9.83×10^{-06}	8.33×10^{-04}
Spouting Spring-Tao1	1.80×10^{-03}	8.44×10^{-04}	-1.38×10^{-02}	5.75×10^{-03}	2.30×10^{-02}	3.22×10^{-02}	-5.31×10^{-03}	-1.32×10^{-03}	0
Tao1-GR2	4.86×10^{-04}	9.62×10^{-04}	-4.27×10^{-04}	-4.10×10^{-04}	2.70×10^{-03}	3.04×10^{-02}	-2.78×10^{-03}	-7.24×10^{-04}	0

[a]Note: Positive and negative values represent the amount of dissolution and precipitation, respectively.

https://doi.org/10.1021/acsomega.4c02870
ACS Omega 2024, 9, 36299−36313

Table 4. Statistical Table of the SI of Major Mineral Phases

Sample category	Sample number	Anhydrite	Aragonite	Calcite	Dolomite	Gypsum	Halite
Carbonate rock thermal reservoir geothermal water	T2	−0.13	0.42	0.56	0.79	0.01	−4.26
	T3	−0.16	0.41	0.55	0.78	−0.02	−4.27
	T4	−0.12	0.37	0.5	0.68	0	−4.26
	TS1	−0.19	0.31	0.44	0.61	−0.01	−4.77
	TS2	−0.2	0.94	1.08	1.92	−0.03	−4.78
	TS3	−0.21	0.44	0.58	0.88	−0.06	−4.77
	TS4	−0.79	0.75	0.88	1.56	−0.62	−5.63
	TR1	−0.08	0.78	0.91	1.56	−0.07	−5.78
	TR2	−0.12	0.44	0.58	0.94	0	−6.55
	TR3	−0.36	0.87	1.01	1.77	−0.18	−6.63
	TR4	−0.19	0.9	1.03	1.78	−0.08	−6.05
	TR5	−0.06	0.52	0.64	1.02	−0.05	−5.84
	TR6	−0.03	0.55	0.67	1.09	−0.01	−6.48
	TR7	−0.77	0.8	0.93	0.73	−0.62	−6.73
Intrusive rock thermal reservoir geothermal water	QR1	−1.94	−0.32	−0.46	−0.52	−1.72	−7.16
	QR2	−2.24	−0.5	−0.64	−1.43	−2.03	−8.11
Southern cold water	NKEZ	−1.82	−0.6	−0.16	−1.11	−1.57	−8.80
	Spouting Spring	−1.87	−0.24	−0.11	−0.22	−1.62	−7.72
	Black Tiger Spring	−1.72	−0.5	−0.25	−0.79	−1.48	−7.41

Table 5. Hydrogen and Oxygen Isotope Data Sheet for the Study Area

Sample category	Sample number	h (m)	δD (‰)	$\delta^{18}O$ (‰)	H_1 (m)	H_2 (m)	$\bar{H}$ (m)
Carbonate rock thermal reservoir geothermal water	T2	23	−69.00	−9.30	887.10	914.00	900.55
	T3	22	−71.00	−9.30	1048.39	1075.20	1061.79
	T4	22	−69.00	−9.30	887.10	914.00	900.55
	TS1	22	−72.00	−9.70	1129.03	1155.80	1142.42
	TS3	22	−72.00	−9.80	1129.03	1155.80	1142.42
	TS4	24	−66.50	−9.20	685.48	712.50	698.99
	TR1	21	−76.00	−10.50	1451.61	1478.20	1464.91
	TR4	25	−76.00	−10.00	1451.61	1478.20	1464.91
	TR5	23	−75.40	−10.20	1403.23	1429.84	1416.53
	TR7	27	−68.00	−9.70	806.45	833.40	819.93
Intrusive rock thermal reservoir geothermal water	QR1	28	−72.00	−9.60	1129.03	1155.80	1142.42
	QR2	29	−70.50	−9.40	1008.06	1034.90	1021.48

groundwater burial, the groundwater is in a closed environment and $CO_2(g)$ is no longer involved in the reaction.

From TS1 to T4, the groundwater burial depth is further increased and the runoff is stagnant. Due to the relatively short path, the water−rock interaction is significantly weakened compared with the previous path. Dolomite begins to precipitate, indicating that calcite is less soluble than dolomite. The precipitation and solubility of other minerals are significantly weakened, and the overall reaction type is basically the same.

The simulation results of the reaction path, to some extent, indicate that geothermal water is accompanied by the dissolution−precipitation phenomenon of minerals during the transportation process and that geothermal water originates from the southern part of the study area.

4.3. Mineral Dissolution Equilibrium. In order to further verify the water−rock interaction and mineral dissolution−precipitation occurring in geothermal water, the equilibrium dissolution−precipitation state of the mineral phase is calculated, and the saturation indices (SI) of various minerals in water samples are obtained.

$$SI = \log(IAP/K_T) \quad (10)$$

where IAP is the product of the activities of the anions and cations comprising a mineral in aqueous solution, and K_T is the thermodynamic equilibrium constant of the mineral at the measured temperature. When SI > 0, the mineral is supersaturated in groundwater; when SI < 0, the mineral is unsaturated in groundwater; when SI = 0, the mineral is in equilibrium.[53]

The SI of different minerals (anhydrite, aragonite, calcite, dolomite, gypsum, and halite) is calculated using PHREEQC software, and the calculation results are shown in Table 4. The SI of sulfate minerals (gypsum, anhydrite) and halite in the collected samples are negative and in the unsaturated state. Moreover, their SI value tends to increase from southern cold water to northern geothermal water, which further indicates that the effects of rock weathering and mineral dissolution are gradually decreasing and are not the primary factors controlling the change of ionic concentration in geothermal water. During the transport of groundwater from south to north, carbonate minerals (aragonite, calcite, dolomite) gradually transition from an unsaturated dissolved state to a saturated precipitated state. This is due to a gradual increase in the degree of evaporation-concentration and cation ($Na^+(K^+)$-$Ca^{2+}(Mg^{2+})$) exchange, which saturates the groundwater with CO_3^{2-}, leading to precipitation in the form of a precipitate.[27]

https://doi.org/10.1021/acsomega.4c02870
ACS Omega 2024, 9, 36299−36313

Therefore, according to the calculation results of mineral SI, the concentration of $Na^+(K^+)$, Cl^-, and SO_4^{2-} in geothermal water increases continuously due to the effect of evaporation and concentration during the northward runoff of groundwater. As the carbonate minerals reach the saturated precipitation state, the growth rate of Ca^{2+} concentration decreases, the concentration of Mg^{2+} and HCO_3^- decreases, and the TDS in the aquifer increases, which is basically consistent with the results of PC1 and the Gibbs diagram above.

4.4. Exploration of Karst Geothermal Genesis. *4.4.1. Geothermal Fluid Recharge Sources.* Stable isotope ratios are valuable tools for identifying the origin, and runoff processes.[14,48] Table 5 presents the stable isotope values of geothermal water samples in the study area, with δD values ranging from −66.50 to −76.00‰ and $\delta^{18}O$ values from −9.20 to −10.50‰. Figure 9 illustrates the correlation between the

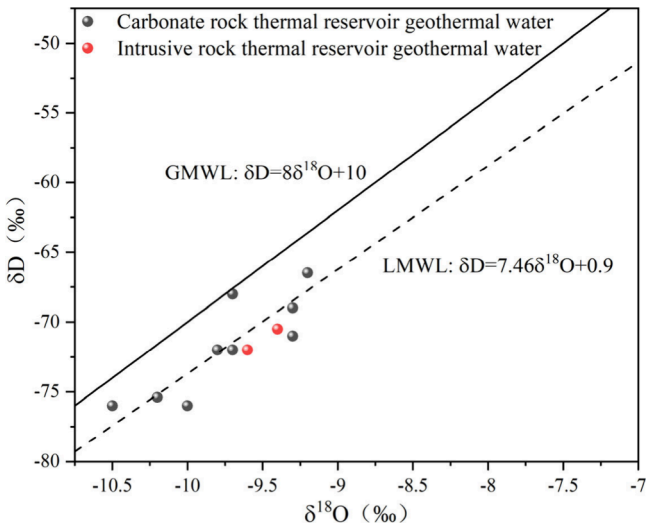

Figure 9. Relationship between δD and $\delta^{18}O$ in geothermal water and the global mesowater line (GMWL) and the local meteoric water line (LMWL) in northern Jinan.

δD and $\delta^{18}O$ values of the geothermal water samples in the study area with the global meteoric water line (GMWL, $\delta D = 8 \times \delta^{18}O + 10$)[54] and the local meteoric water line (LMWL, $\delta D = 7.5 \times \delta^{18}O + 5.4$).[55] It can be seen that the geothermal water samples are all located below the GMWL, indicating that the recharge source of geothermal water is relatively single but basically distributed along the LMWL, indicating that the direct recharge source of geothermal water is atmospheric precipitation. The elevation of the source area of geothermal water can be calculated according to eqs 11 and 12 of the altitude effect of stable isotopes.

Method 1: Equation for calculating the recharge elevation of $\delta^{18}O$ values in groundwater in relation to local elevation:[27]

$$H_1 = h + \frac{D - D_r}{\text{grad } D} \quad (11)$$

Method 2: Elevation effect equation for δD values of atmospheric precipitation in Jinan:[55]

$$H_2 = -80.6 \cdot D - 4647.4 \quad (12)$$

In the equation, H and h represent the elevation of the recharge area of geothermal water and the sampling point of geothermal water, respectively, measured in meters. D and D_r denote the δD value of the geothermal water sample and atmospheric precipitation, respectively, measured in per mil (‰). grad D represents the elevation gradient of the δD value with respect to altitude, measured in millimeters per meter (‰/m).

The elevation of the sampling points in the study area is 22−29 m.s.a.l. The mean value of −58‰ was used for the δD value of atmospheric precipitation, and the elevation δD gradient is −1.24‰/100 m. Table 5 shows that the results of H_1 and H_2 calculations are similar, and both are applicable to the study area. Therefore, the average value ($\bar{H}$) is taken as the recharge zone elevation of the study area, which is 698.99−1464.91 m.s.a.l. It is inferred that the recharge zone is the Taiyi Mountain in the south.

In summary, the source of karst geothermal water in the study area is the infiltration and recharge of atmospheric precipitation in the Taiyi Mountain. After being heated by the upper mantle conduction heat flow, it is blocked by the water-insulating rock layer, rises to the shallow aquifer along the deep fracture, and is stored in the thermal reservoir under the heat-blocking and heat-insulating effect of the overlying huge-thick cover of loose sediments.

4.4.2. Estimation of Thermal Reservoir Temperature. First, the water−rock equilibrium state of the geothermal water was determined by Na−K−Mg triangulation.[56] In Figure 10, all of

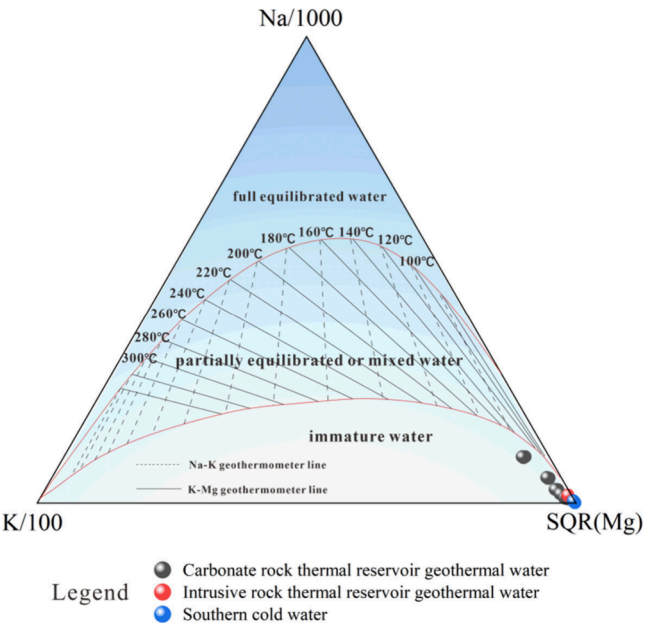

Figure 10. Na−K−$Mg^{1/2}$ ternary diagram for the water samples in the study area.

the geothermal water samples in the study area are located in the immature water zone, which represents the mixing of geothermal water with surface infiltrated cold water during its ascent along the fracture channel, reducing the maturity of the geothermal water, and the limitation of using the cation temperature scale method, which makes it suitable for estimation using the SiO_2 temperature scale method.

In geothermal chemistry, common SiO_2 minerals include quartz, chalcedony, amorphous SiO_2, α-cristobalite and β-cristobalite, and the dissolved state of minerals can be judged by the relationship between SiO_2 and K^2/Mg.[57,58] As shown in

https://doi.org/10.1021/acsomega.4c02870
ACS Omega 2024, 9, 36299−36313

Figure 11, some of the water sample points are distributed between quartz and chalcedony lines, and most of the water

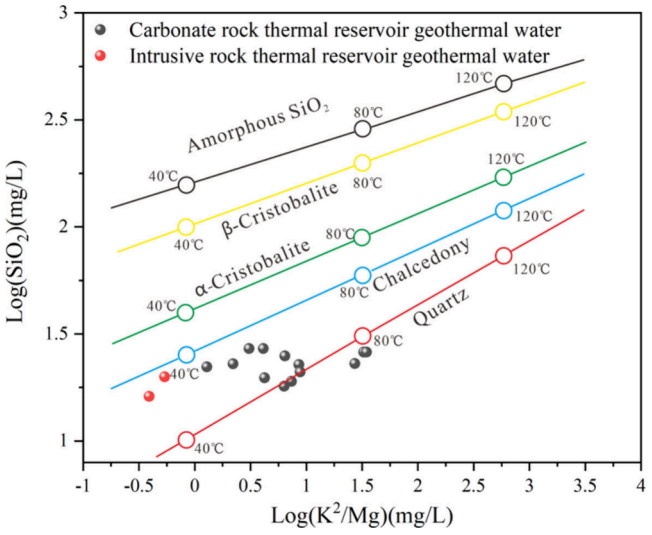

Figure 11. Plot of log(SiO_2) versus log(K^2/Mg), concentrations in milligrams per liter. Lines indicate the temperature dependence of the variables for silica minerals.

sample points are located near the quartz line, indicating that SiO_2 in the geothermal water in the study area is mainly controlled by quartz and chalcedony dissolution. In this paper, quartz and chalcedony chemical geothermometers are selected to estimate the thermal reservoir temperature in the study area. most of the reservoir temperatures shown by the SiO_2 versus K^2/Mg curves are in the range 40−80 °C. The temperature of the reservoirs in the study area is in the range 40−80 °C.

Using quartz and chalcedony chemical geothermometers, we calculated the thermal reservoir temperatures at each sampling point in the study area according to eqs 5 and 6, which ranged from 55.62 to 98.16 °C and 23.27−67.97 °C (Table 6), respectively. It should be noted that there is a small amount of

Table 6. Reservoir Temperatures Were Estimated Using Selected Chemical Geothermometers[a]

Sample category	Sample	Observed temperature	Quartz, no steam loss	Chalcedony
Carbonate rock thermal reservoir geothermal water	T2	39.0	73.60	41.96
	T3	40.0	68.78	36.92
	T4	43.0	73.60	41.96
	TS1	33.0	61.53	29.38
	TS2	36.0	59.53	27.31
	TS3	38.0	68.36	36.48
	TS4	35.7	62.97	30.88
	TR1	56.0	71.97	40.25
	TR2	43.0	68.61	36.74
	TR3	33.0	67.43	35.51
	TR4	43.2	75.11	43.55
	TR5	57.0	75.11	43.55
	TR6	55.5	–	–
	TR7	38.0	65.29	33.28
Intrusive rock thermal reservoir geothermal water	QR1	25.2	98.16	67.97
	QR2	27.5	55.62	23.27

[a]Note: – are no available data, units for temperature are °C.

cold water mixing during the formation of geothermal water; therefore, the estimated thermal reservoir temperature should be greater than the measured temperature. Therefore, upon comparison of the calculated results with the measured temperatures, it can be seen that the estimated temperatures of the quartz geothermometer are more in line with the reality.

Quartz, (no steam loss) geothermometer:[57]

$$T = \frac{1309}{5.19 - \lg SiO_2} - 273.15 \quad (13)$$

Chalcedony geothermometer:[57]

$$T = \frac{1032}{4.69 - \lg SiO_2} - 273.15 \quad (14)$$

4.4.3. Conceptual Modeling of Karst Geothermal Water Flow Systems. The cap rocks of the karst geothermal water flow system in the study area are Quaternary, Neoproterozoic, Permian, and Carboniferous. The primary heat source originates from deep crustal heat flow and is conducted upward through deep faults. The source of geothermal water supply is the atmospheric precipitation infiltration in the exposed mountainous area of southern limestone, and it flows from the south to the north along the inclination of rock strata and the slope direction of strata. Part of the karst water is blocked by Jinan rock mass, forming spring group flow, such as Spouting Spring and Black Tiger Spring. The other part of karst water will continue to flow along the karst fissure channels and fracture zones to the deep karst aquifers in the north and eventually be stored in the Ordovician-Cambrian aquifers, with a reservoir temperature of 55.62−98.16 °C, forming the Ordovician-Cambrian karst geothermal field. Based on the geological background of the geothermal field in the study area, the evolution process of geothermal fluids, and the recharge of water sources, a model for the genesis of the karst geothermal water flow system is proposed (Figure 12).

5. CONCLUSIONS

(1) Groundwater hydrochemistry type from southern cold water to northern geothermal water shows obvious zoning characteristics, as evidenced by the evolution from HCO_3−Ca type to HCO_3−Ca−Mg type, and then further evolved to SO_4−Ca and SO_4−Ca−Na type water. The cold water in the south is more shallowly buried, and the hydrochemical characteristics of the groundwater are more stable. The higher TDS content of geothermal water in the north indicates a relatively closed hydrogeochemical environment with slow runoff.

(2) Along the direction of groundwater runoff, the main controlling factor affecting the chemical components of groundwater shifts from rock weathering to evaporation−concentration action. Carbonate, sulfate, silicate minerals, and rock salts are dissolution−precipitation is an important hydrogeochemical process controlling the hydrochemical characteristics of groundwater in this area. Gypsum gradual dissolution inhibits dolomite and calcite dissolution and further leads to their precipitation.

(3) Using δD and $\delta^{18}O$ stable isotopes, the geothermal water recharge elevation is calculated to be 698.99−1464.91 m.s.a.l., and it is inferred that the recharge area is the Taiyi mountainous area in the south, which belongs to

https://doi.org/10.1021/acsomega.4c02870
ACS Omega 2024, 9, 36299−36313

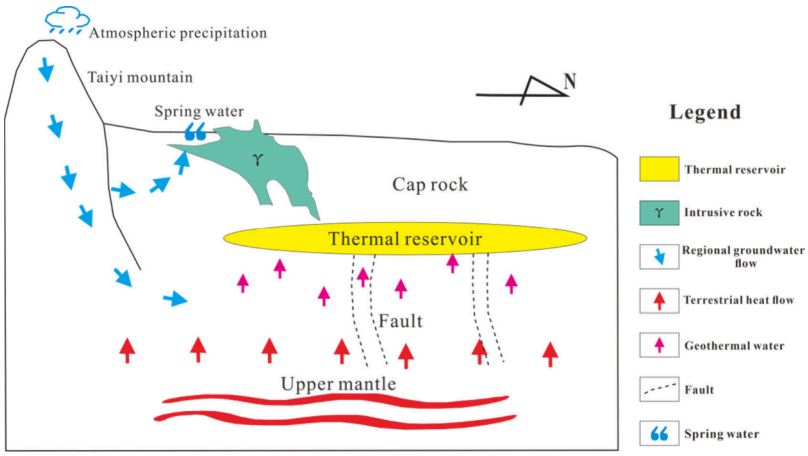

Figure 12. Genetic model of the karst geothermal water flow system.

the infiltration of atmospheric precipitation. The temperature of the thermal reservoir was estimated to be 55.62−98.16 °C by using Na−K−Mg triangulation and chemical geothermometer.

(4) Based on the geological background of the geothermal field in the study area, the process of geothermal fluid evolution, and the recharge of water sources, a model of the genesis of the karst geothermal water flow system was established. It enriches the study of karst geothermal system and is of great scientific significance in guiding the development, utilization and planning of karst geothermal resources from the perspective of the genesis of geothermal resources and hydrochemical characteristics.

AUTHOR INFORMATION

Corresponding Author

Wei Zhou − *College of Earth Science and Engineering and Shandong Provincial Key Laboratory of Depositional Mineralization & Sedimentary Mineral, Shandong University of Science and Technology, Qingdao, Shandong 266590, China*; orcid.org/0009-0001-6702-2664; Email: 19862255301@163.com

Authors

Shuchun Wang − *Shandong Geology and Mineral Engineering Group Co., Ltd., Jinan 250200, China*

Zhiqing Liu − *Shandong Geology and Mineral Engineering Group Co., Ltd., Jinan 250200, China*

Yanyu Jiang − *Shandong Geology and Mineral Engineering Group Co., Ltd., Jinan 250200, China*

Hongliang Ding − *Shandong Geology and Mineral Engineering Group Co., Ltd., Jinan 250200, China*

Fangying Dong − *College of Earth Science and Engineering and Shandong Provincial Key Laboratory of Depositional Mineralization & Sedimentary Mineral, Shandong University of Science and Technology, Qingdao, Shandong 266590, China*

Complete contact information is available at: https://pubs.acs.org/10.1021/acsomega.4c02870

Author Contributions

S.W.: conceptualization, planning, supervision. Z.L.: methodology, formal analysis. W.Z.: methodology, writing—review and editing. Y.J.: data curation, validation. H.D.: visualization, methodology. F.D.: software, data collection.

Notes

The authors declare no competing financial interest.

ACKNOWLEDGMENTS

The work was supported by the project "Investigation of Geothermal Resources in Jinan City and Surrounding Areas". The authors thank all the researchers for their help.

REFERENCES

(1) Agemar, T.; Weber, J.; Moeck, I. S. Assessment and public reporting of geothermal resources in germany: review and outlook. *Energies.* **2018**, *11* (2), 332−332.

(2) Spittler, N.; Davidsdottir, B.; Shafiei, E.; Leaver, J.; Asgeirsson, E. I.; Stefansson, H. The role of geothermal resources in sustainable power system planning in Iceland. *Renew. Energy* **2020**, *153*, 1081−1090.

(3) Baumann, T.; Bartels, J.; Lafogler, M.; Wenderoth, F. Assessment of heat mining and hydrogeochemical reactions with data from a former geothermal injection well in the Malm aquifer, Bavarian Molasse Basin, Germany. *Geothermics* **2017**, *66*, 50−60.

(4) Blasco, M.; Auqué, L. F.; Gimeno, M. J.; Acero, P.; Asta, M. P. Geochemistry, geothermometry and influence of the concentration of mobile elements in the chemical characteristics of carbonate-evaporitic thermal systems. The case of the Tiermas geothermal system (Spain). *Chem. Geol.* **2017**, *466*, 696−709.

(5) Davraz, A.; Aksever, F.; Afsin, M. Assessment of stream water chemistry and impact of geothermal fluid in the up-Buyuk Menderes Basin, Turkey. Environ. *Sci. Pollut. R.* **2017**, *24* (34), 26806−26820.

(6) Etzel, T. M.; Bowman, J. R.; Moore, J. N.; Valley, J. W.; Spicuzza, M. J.; McCulloch, J. M. Oxygen isotope systematics in an evolving geothermal system: Coso Hot Springs, California. *J. Vol. Geoth. Res.* **2017**, *329*, 54−68.

(7) Yin, H.; Zhang, C.; Zhou, X.; Chen, T.; Dong, F.; Cheng, W.; Tang, R.; Xu, G.; Jiao, P. Research on the genetic mechanism of high-temperature groundwater in the geothermal anomalous area of gold deposit—application to the copper mine area of Yinan gold mine. *ACS Omega.* **2022**, *7* (47), 43231−43241.

(8) Chen, N.; Liu, M.; Zhou, W. Fouling and Corrosion Properties of SiO_2 Coatings on Copper in Geothermal Water. *Ind. Eng. Chem. Res.* **2012**, *51* (17), 6001−6017.

(9) Shah, M.; Shah, V.; Dudhat, K.; Patel, D. Evaluation of geothermal water and assessment of corrosive and scaling potential of water samples in Tulsishyam Geothermal Region, Gujarat, India. *Environ. Sci. Pollut. R.* **2023**, *30* (15), 44684−44696.

(10) Kumar, P.; Kumar, A.; Singh, C. K.; Saraswat, C.; Avtar, R.; Ramanathan, A. L.; Herath, S. Hydrogeochemical Evolution and

Appraisal of Groundwater Quality in Panna District, Central India. *Expos. Health.* **2016**, *8* (1), 19−30.
(11) Singh, R.; Syed, T. H.; Kumar, S.; Kumar, M.; Venkatesh, A. S. Hydrogeochemical assessment of surface and groundwater resources of Korba coalfield, Central India: environmental implications. *Arab. J. Geosci.* **2017**, *10* (14), 318.
(12) Liu, J.; Wang, H.; Jin, D.; Xu, F.; Zhao, C. Hydrochemical characteristics and evolution processes of karst groundwater in Carboniferous Taiyuan formation in the Pingdingshan coalfield. *Environ. Earth. Sci.* **2020**, *79* (6), 151.
(13) Zhang, H.; Xu, G.; Chen, X.; Mabaire, A.; Zhou, J. S.; Zhang, Y.; Zhang, G.; Zhu, L. Groundwater hydrogeochemical processes and the connectivity of multilayer aquifers in a coal mine with karst collapse columns. *Mine. Water. Environ.* **2020**, *39* (2), 356−368.
(14) Ismail, E.; Abdelhalim, A.; Ali, A.; Ahmed, M. S.; Scholger, R.; Khalil, M. M. Isotopic, geophysical, and hydrogeochemical investigations of groundwater in west middle upper egypt. *ACS Omega.* **2022**, *7* (48), 44000−44011.
(15) Yang, L.; Liu, L.; Liu, Y.; Chen, G.; Liang, L. Hydrodynamic Groundwater Modeling and Hydrochemical Conceptualization of the Closure Mining Area of the WuMa River Watershed of China. *ACS Omega.* **2024**, *9* (1), 520−537.
(16) Wu, J.; Li, P.; Wang, D.; Ren, X.; Wei, M. Statistical and multivariate statistical techniques to trace the sources and affecting factors of groundwater pollution in a rapidly growing city on the Chinese Loess Plateau. *Hum. Ecol. Risk. Assess.* **2020**, *26* (6), 1603−1621.
(17) Karunanidhi, D.; Subramani, T.; Roy, P. D.; Li, H. Impact of groundwater contamination on human health. *Environ. Geochem. Hlth.* **2021**, *43* (2), 643−647.
(18) Masindi, K.; Abiye, T. Assessment of natural and anthropogenic influences on regional groundwater chemistry in a highly industrialized and urbanized region: a case study of the Vaal River Basin, South Africa. *Environ. Earth. Sci.* **2018**, *77* (20), 722.
(19) Xiao, Y.; Hao, Q.; Zhang, Y.; Zhu, Y.; Yin, S.; Qin, L.; Li, X. Investigating sources, driving forces and potential health risks of nitrate and fluoride in groundwater of a typical alluvial fan plain. *Sci. Total Environ.* **2022**, *802*, 149909.
(20) Zhang, X.; Guo, Q.; Liu, M.; Luo, J.; Yin, Z.; Zhang, C.; Zhu, M.; Guo, W.; Li, J.; Zhou, C. Hydrogeochemical processes occurring in the hydrothermal systems of the Gonghe-Guide basin, northwestern China: critical insights from a principal components analysis (PCA). *Environ. Earth. Sci.* **2016**, *75* (16), 1187.
(21) Alsemgeest, J.; Auque, L. F.; Gimeno, M. J. Verification and comparison of two thermodynamic databases through conversion to PHREEQC and multicomponent geothermometrical calculations. *Geothermics* **2021**, *91*, 102036.
(22) Holmes, N.; Tyrer, M.; West, R.; Lowe, A.; Kelliher, D. Using PHREEQC to model cement hydration. *Constr. Build. Mater.* **2022**, *319*, 126129.
(23) Maréchal, J. C.; Ladouche, B.; Dorfliger, N.; Lachassagne, P. Interpretation of pumping tests in a mixed flow karst system. *Water Resour. Res.* **2008**, DOI: 10.1029/2007WR006288.
(24) Li, C.; Zhao, Y.; Wang, S.; Zhang, H. Analysis of the rules of water enrichment in the geothermal field northern Jinan Shandong Province. *Earth Environ.* **2008**, No. 02, 155−160.
(25) Hartmann, A.; Goldscheider, N.; Wagener, T.; Lange, J.; Weiler, M. Karst water resources in achanging world: review of hydrological modeling approaches. *Rev. Geophys.* **2014**, *52*, 218−242.
(26) Liñán Baena, C.; Andreo, B.; Mudry, J.; Carrasco, C. Groundwater temperature and electrical conductivity as tools to characterize flow patterns in carbonate aquifers: The Sierra de las Nieves karst aquifer, southern Spain. *Hydrogeol. J.* **2009**, *17* (4), 843−853.
(27) Dong, F.; Yin, H.; Cheng, W.; Li, Y.; Qiu, M.; Zhang, C.; Tang, R.; Xu, G.; Zhang, L. Study on water inrush pattern of Ordovician limestone in North China Coalfield based on hydrochemical characteristics and evolution processes: A case study in Binhu and Wangchao Coal Mine of Shandong Province, China. *J. Clean. Prod.* **2022**, *380*, 134954.
(28) Xiao, J.; Lv, G.; Chai, N.; Hu, J.; Jin, Z. Hydrochemistry and source apportionment of boron, sulfate, and nitrate in the Fen River, a typical loess covered area in the eastern Chinese Loess Plateau. *Environ. Res.* **2022**, *206*, 112570.
(29) Li, X.; Xiao, J.; Chai, N.; Jin, Z. Controlling mechanism and water quality assessment of arsenic in China's Yellow River Basin. *J. Clean. Prod.* **2023**, *418*, 137953.
(30) Wu, J.; Li, P.; Qian, H.; Duan, Z.; Zhang, X. Using correlation and multivariate statistical analysis to identify hydrogeochemical processes affecting the major ion chemistry of waters: a case study in Laoheba phosphorite mine in Sichuan, China. *Arab. J. Geosci.* **2014**, *7* (10), 3973−3982.
(31) Salem, N.; Hussein, S. Data dimensional reduction and principal components analysis. *Procedia Computer Science* **2019**, *163*, 292−299.
(32) Hizli, S.; Karaoglu, A. G.; Goren, A. Y.; Kobya, M. Identifying Geogenic and Anthropogenic Aluminum Pollution on Different Spatial Distributions and Removal of Natural Waters and Soil in Canakkale, Turkey. *ACS Omega* **2023**, *8*, 8557.
(33) Cloutier, V.; Lefebvre, R.; Therrien, R.; Savard, M. M. Multivariate statistical analysis of geochemical data as indicative of the hydrogeochemical evolution of groundwater in a sedimentary rock aquifer system. *J. Hydrol.* **2008**, *353* (3), 294−313.
(34) Li, W.; Wu, J.; Zhou, C.; Nsabimana, A. Groundwater pollution source identification and apportionment using PMF and PCA-APCS-MLR receptor models in Tongchuan City, China. Arch. Environ. *Con. Tox.* **2021**, *81* (3), 397−413.
(35) Jia, Z.; Zang, H.; Hobbs, P.; Zheng, X.; Xu, Y.; Wang, K. Application of inverse modeling in a study of the hydrogeochemical evolution of karst groundwater in the Jinci Spring region, northern China. *Environ. Earth. Sci.* **2017**, *76* (8), 312.
(36) Fu, C.; Zhang, W.; Zhang, S.; Su, X.; Lin, X. Identifying key hydrochemical processes in a confined aquifer of an arid basin using multivariate statistical analysis and inverse modeling. *Environ. Earth. Sci.* **2014**, *72* (1), 299−310.
(37) Zhang, M.; Chen, L.; Yao, D.; Hou, X.; Zhang, J.; Qin, H.; Ren, X.; Zheng, X. Hydrogeochemical processes and inverse modeling for a multilayer aquifer system in the Yuaner coal mine, Huaibei coalfield, China. *Mine. Water. Environ.* **2022**, *41* (3), 775−789.
(38) Piper, A. M. A graphic procedure in the geochemical interpretation of water-analyses. *Eos, Trans. Am. Geophys. Union* **1944**, DOI: 10.1029/TR025i006p00914.
(39) Yang, F.; Liu, S.; Jia, C.; Gao, M.; Chang, W.; Wang, Y. Hydrochemical characteristics and functions of groundwater in southern Laizhou Bay based on the multivariate statistical analysis approach. *Estuar. Coast. Shelf. Sci.* **2021**, *250*, 107153.
(40) Liu, J.; Peng, Y.; Li, C.; Gao, Z.; Chen, S. An investigation into the hydrochemistry, quality and risk to human health of groundwater in the central region of Shandong Province, North China. *J.Clean. Prod.* **2021**, *282*, 125416.
(41) Liu, L.; Wu, J.; He, S.; Wang, L. Occurrence and distribution of groundwater fluoride and manganese in the Weining Plain (China) and their probabilistic health risk quantification. *Expos. Health.* **2022**, *14* (2), 263−279.
(42) Raidla, V.; Kirsimaee, K.; Ivask, J.; Kaup, E.; Knöller, K.; Marandi, A.; Martma, T.; Vaikmäe, R. Sulphur isotope composition of dissolved sulphate in the Cambrian-Vendian aquifer system in the northern part of the Baltic Artesian Basin. *Chem. Geol.* **2014**, *383*, 147−154.
(43) Wang, J.; Jin, M.; Jia, B.; Kang, F. Hydrochemical characteristics and geothermometry applications of thermal groundwater in northern Jinan, Shandong, China. *Geothermics.* **2015**, *57*, 185−195.
(44) Chatterjee, S.; Sinha, U. K.; Biswal, B. P.; Jaryal, A.; Jain, P.; Patbhaje, S.; Dash, A. An Integrated Isotope-Geochemical Approach to Characterize a Medium Enthalpy Geothermal System in India. *Aquat. Geochem.* **2019**, *25* (1−2), 63−89.

https://doi.org/10.1021/acsomega.4c02870
ACS Omega 2024, 9, 36299−36313

(45) Xu, P.; Zhang, Q.; Qian, H.; Li, M.; Hou, K. Characterization of geothermal water in the piedmont region of Qinling Mountains and Lantian-Bahe Group in Guanzhong Basin, China. *Environ. Earth. Sci.* **2019**, *78* (15), 442.
(46) Mukherjee, A.; Bhattacharya, P.; Shi, F.; Fryar, A. E.; Mukherjee, A. B.; Xie, Z.; Jacks, G.; Bundschuh, J. Chemical evolution in the high arsenic groundwater of the Huhhot basin (Inner Mongolia, PR China) and its difference from the western Bengal basin (India). *Appl. Geochem.* **2009**, *24* (10), 1835−1851.
(47) Gaillardet, J.; Dupré, B.; Louvat, P.; Allègre, C. J. Global silicate weathering and CO_2 consumption rates deduced from the chemistry of large rivers. *Chem. Geol.* **1999**, *159* (1), 3−30.
(48) Yin, H.; Zhou, W.; Dong, F.; Liu, Y.; Shi, C.; Meng, M.; Cheng, W. Hydrochemical characteristics and genetic mechanism of porous sandstone geothermal water in northern Jinan, Shandong, China. *Environ. Sci. Pollut. Res.* **2024**, *31*, 24180−24196.
(49) Lindsey, C. R.; Neupane, G.; Spycher, N.; Fairley, J.; Dobson, P.; Wood, T.; McLing, T.; Conrad, M. Cluster analysis as a tool for evaluating the exploration potential of Known Geothermal Resource Areas. *Geothermics.* **2018**, *72*, 358−370.
(50) Gibbs, R. J. Mechanisms Controlling World Water Chemistry. *Science.* **1970**, *170* (3962), 1088−1090.
(51) Ravish, S.; Setia, B.; Deswal, S. Data on appraisal of groundwater quality in north-eastern Haryana. *Data. Brief.* **2019**, *25*, 104164−104164.
(52) Sung, K.; Yun, S.; Park, M.; Koh, Y. K.; Choi, B. Y.; Hutcheon, I.; Kim, K. H. Reaction path modeling of hydrogeochemical evolution of groundwater in granitic bedrocks, South Korea. *J. Geochem. Explor.* **2012**, *118*, 90−97.
(53) Chen, Q.; Jia, C.; Wei, J.; Dong, F.; Yang, W.; Hao, D.; Jia, Z.; Ji, Y. Geochemical process of groundwater fluoride evolution along global coastal plains: Evidence from the comparison in seawater intrusion area and soil salinization area. *Chem. Geol.* **2020**, *552*, 119779.
(54) Craig, H. Isotopic Variations in Meteoric Waters. *Science.* **1961**, *133* (3465), 1702−1703.
(55) Liu, J.; Song, X.; Yuan, G.; Sun, X.; Liu, X.; Wang, S. Characteristics and water vapor sources of atmospheric precipitation $\delta^{18}O$ in the monsoon region of eastern China. *Sci. Bull.* **2009**, *54* (22), 3521−3531.
(56) Giggenbach, W. F. Geothermal solute equilibria. Derivation of Na-K-Mg-Ca geoindicators. *Geochim. Cosmochim. Ac.* **1988**, *52* (12), 2749−2765.
(57) Fournier, R. O. Chemical geothermometers and mixing models for geothermal systems. *Geothermics.* **1977**, *5* (1−4), 41−50.
(58) Giggenbach, W.; Sheppard, D. S.; Robinson, B. W.; Stewart, M. K.; Lyon, G. L. Geochemical structure and position of the Waiotapu geothermal field, New Zealand. *Geothermics* **1994**, *23* (5−6), 599−644.

https://doi.org/10.1021/acsomega.4c02870
ACS Omega 2024, 9, 36299−36313